The resolution sensitivity of the Asian summer monsoon and its inter-model comparison between MRI-AGCM and MetUM

Article

Accepted Version

To link to this article DOI: http://dx.doi.org/10.1007/s00382-016-3517-5

Publisher: Springer

The Resolution Sensitivity of the Asian Summer Monsoon and its Inter-Model Comparison between MRI-AGCM and MetUM

Tomomichi Ogata[1],

Stephanie J. Johnson[2], Reinhard Schiemann[2], Marie-Estelle Demory[2],

Ryo Mizuta[3], Kohei Yoshida[3], Osamu Arakawa[1, 3]

[1]Faculty of Life and Environmental Sciences, University of Tsukuba, Japan

[2]National Centre for Atmospheric Science, Department of Meteorology, University of Reading, UK

[3]Meteorological Research Institute, Tsukuba, Japan

Submitted to Climate Dynamics

December 2016

Abstract

In this study, we compare the resolution sensitivity of the Asian Summer Monsoon (ASM) in two Atmospheric General Circulation Models (AGCMs): the MRI-AGCM and the MetUM. We analyze the MetUM at three different resolutions, N96 (approximately 200-km mesh on the equator), N216 (90-km mesh) and N512 (40-km mesh), and the MRI-AGCM at TL95 (approximately 180-km mesh on the equator), TL319 (60-km mesh), and TL959 (20-km mesh). The MRI-AGCM and the MetUM both show decreasing precipitation over the western Pacific with increasing resolution, but their precipitation responses differ over the Indian Ocean. In MRI-AGCM, a large precipitation increase appears off the equator (5-20°N). In MetUM, this off-equatorial precipitation increase is less significant and precipitation decreases over the equator. Moisture budget analysis demonstrates that a changing in moisture flux convergence at higher resolution is related to the precipitation response. Orographic effects, intra-seasonal variability and the representation of the meridional thermal gradient are explored as possible causes of the resolution sensitivity. Both high-resolution AGCMs (TL959 and N512) can represent steep topography, which anchors the rainfall pattern over south Asia and the Maritime Continent. In MRI-AGCM, representation of low pressure systems in TL959 also contributes to the rainfall pattern. Furthermore, the seasonal evolution of the meridional thermal gradient appears to be more accurate at higher resolution, particularly in the MRI-AGCM. These findings emphasize that the impact of resolution is only robust across the two AGCMs for some features of the ASM, and highlights the importance of multi-model studies of GCM

resolution sensitivity.

1. Introduction

The Asian Summer Monsoon (ASM) is an important component of the global monsoon. Its multi-scale variability, ranging from sub-seasonal to inter-decadal time scales, impacts society through natural disasters and changes in water resources (e.g. Chang et al. 2000, Lau and Kim 2012, He and Zhou 2015, Joseph et al. 2015, Cho et al. 2015). Recent advances in climate simulation have improved the fidelity of the ASM, but large biases remain. Sperber et al. (2013) and Ogata et al. (2014) reported that there is little improvement in Coupled Model Intercomparison Project Phase 5 (CMIP5) General Circulation Models (GCM) seasonal climatology compared to CMIP3 GCMs and there are still substantial biases in the ASM simulations. At inter-annual timescales, the ENSO-Indian monsoon relationship (defined by all-India rainfall and Nino-3.4) is too strong in individual CMIP5 models, while the ENSO-East Asian monsoon relationship is too weak in multi-model mean. CMIP3 and CMIP5 GCMs also commonly exhibit a late monsoon onset (Sperber et al., 2013). At sub-seasonal timescales, CMIP5 GCMs depict a large inter-model spread in the reproducibility of the Boreal Summer Intra-Seasonal Oscillation (BSISO) of about 20-60 day period (e.g. Yasunari 1980, Jiang et al. 2004, Ajayamohan et al. 2009).

The most significant differences between CMIP3 and CMIP5 GCMs are the improvement of physics schemes and the increase in horizontal and vertical resolutions. CMIP results include the model-produced SST bias, which makes the detection of causes of model bias in the ASM simulation difficult. Therefore, an intercomparison of atmospheric GCMs (AGCM) in an “AMIP-style” (Atmospheric Model Intercomparison

Project) configuration, using observed SST and sea-ice boundary conditions, is often more appropriate for diagnosing sources of bias or understanding the reason of response changes in atmospheric models. In this paper, we focus on the effect of only increasing horizontal resolution on the ASM simulation and perform an assessment with two AGCMs.

Development in high-performance computing enables high-resolution AGCMs that can resolve fine-scale orographic effect and synoptic-scale atmospheric variations. Kitoh and Kusunoki (2008) investigated the ASM simulation in a 20-km resolution AGCM and reported that increased resolution of steep orography improved the precipitation climatology (Xie et al. 2006). Other resolution sensitivity studies have shown that orographic precipitation over the Western Ghats and the Indochina peninsula and the wind speed of Somali Jet are generally improved with increasing resolution (Sperber et al. 1994, Jha et al. 2000, Kobayashi and Sugi 2004, Sabin et al. 2013). However, resolution sensitivity of precipitation in other areas such as the western equatorial Indian Ocean and Indian peninsula differs between studies (Sperber et al. 1994, Stephenson et al. 1998, Martin 1999, Sabin et al. 2013).

The 20-60 day BSISO, other intra-seasonal modes of 10-20 days (e.g. Murakami 1976, Krishnamurti and Ardanuy 1980, Annamalai and Slingo 2001) and synoptic 3-5 day Low Pressure Systems (LPS; e.g. Mak 1987, Goswami et al. 2003) all interact on intra-seasonal time scales over the south Asia (Annamalai and Slingo 2001, Goswami et al. 2003). These intra-seasonal variations and its multi-scale interactions are considered as an important factor to the ASM reproducibility in GCMs (e.g. Liu et al.

2009, Sperber et al. 2013, Sabeerali et al. 2013), and it is believed that high-resolution GCMs better simulate such multi-scale interactions (e.g. Roberts et al, 2015; Vellinga et al, 2016). Increasing horizontal resolution is also key to improving simulations of tropical cyclones (TC; e.g. Oouchi et al. 2006, Murakami and Sugi 2010) and has some common effects including improvement of TC distribution and intensity, decrease of weak TC and increase of strong TC in the future climate (Murakami et al. 2012, Roberts et al. 2015).

Each resolution sensitivity study uses slightly different techniques and analyses different aspects of resolution sensitivity. Moreover, it is also well known that a large inter-model spread in the reproducibility of the ASM exists, even in AMIP-style simulations. For example, on the south Asian monsoon, Kitoh and Kusunoki (2008) exhibited that major precipitation maximum locates around 10-20°N in MRI-AGCM at both low and high resolutions. In contrast, Johnson et al. (2016) showed that major precipitation maximum locates over the equator and precipitation around 10-20°N is rather weak in MetUM at both low and high resolutions. In order to understand what aspects of resolution sensitivity are common among GCMs, it is important to conduct a coordinated resolution sensitivity study of multiple AGCMs using the same analysis techniques.

In this study, based on Johnson et al. (2016), we compare the resolution sensitivity of the ASM in two state-of-the-art AGCMs (MRI-AGCM and MetUM). We compare the MetUM integrations at N96 (200-km mesh on the equator), N216 (90-km mesh) and N512 (40-km mesh) that were used by Johnson et al. (2016) with an

MRI-AGCM series at TL95 (180-km mesh on the equator), TL319 (60-km mesh), and TL959 (20-km mesh) resolutions. Johnson et al. (2016) found that fine orography at N512 improves orographic rainfall over the south Asian continent and the Somali Jet wind speed is increased by the better resolution of the East African Highlands. Over the Maritime Continent (MC), rainfall increases over land, while it decreases in the west Pacific. Furthermore, Johnson et al. (2016) investigated the role of LPS on the rainfall change over India and concluded that LPS contribute to slightly more rainfall over northeast India at N512. In this paper, we compare this resolution sensitivity to the sensitivity of the MRI-AGCM, and analyze similarities and differences. Section 2 describes the models used in this study. Section 3 shows the results of the seasonal mean ASM and its resolution sensitivity. Section 4 presents the orographic effects and intraseasonal variability. Upper tropospheric thickness and its seasonal evolution are also investigated as a measurement of drivers of the ASM. Section 5 presents the summary and a discussion of the results.

2. Methodology

2.1. Experiments in MRI-AGCM and MetUM

We make use of the MRI-AGCM3.2 model (Mizuta et al. 2012) developed at 20-km and 60-km horizontal resolutions, with 64 vertical levels (TL959L64 and TL319L64). This model, in which an especially deep convective scheme was changed from a relaxed Arakawa–Schubert scheme to a Tiedtke-like scheme proposed by

Yoshimura et al. (2015), is an improved version of MRI-AGCM3.1 (Mizuta et al. 2006). Using the 20-km resolution AGCM (MRI-AGCM3.2S), Murakami et al. (2012) reported that the simulated intensity of global TCs was significantly improved, as compared with results of the previous version (MRI-AGCM3.1S). These 20-km and 60-km AGCMs are used for studies of TCs (Murakami et al. 2012), global monsoon (Endo et al. 2012) and East Asian monsoon (Kusunoki and Mizuta 2013) in the future climate. An additional simulation of MRI-AGCM3.2 at 180-km horizontal resolution (TL95L64) was performed for resolution sensitivity studies. In MRI-AGCM, the lower boundary conditions are prescribed by observed monthly-mean SST and sea ice concentration of the Met Office Hadley Centre Sea Ice and Sea Surface Temperature version 1 (HadISST1; Rayner et al. 2003) for the period 1979–2003. To focus on resolution sensitivity, we only changed the horizontal resolution while other settings (i.e. vertical resolution and physical package) remain the same.

The configuration of the MetUM used here is the Global Atmosphere 3.0 (Walters et al. 2011) configuration of the atmospheric component of the HadGEM3 family. We used integrations from the UPSCALE simulation campaign (Mizielinski et al. 2014) at three horizontal resolutions: approximately 40-km, 90-km and 200-km, and 85 vertical levels (N512L85, N216L85, N96L85 respectively). The lower boundary conditions are prescribed by the observed daily-mean SST and sea ice concentration of the OSTIA product (Donlon et al. 2012) for the period 1985–2011. The UPSCALE campaign simulations have previously been used for multiple resolution sensitivity studies, such as the global and regional hydrological cycles (Demory et al. 2014;

Schiemann et al. 2014; Vellinga et al. 2016), ASM (Johnson et al. 2016) and TCs (Roberts et al. 2015). Similar to MRI-AGCM, only horizontal resolution was changed between integrations. A detailed description of the integrations and model settings is given in Mizielinski et al. (2014).

2.2. Observational datasets

The Japanese 55-year reanalysis (JRA-55, Kobayashi et al. 2015, 1.25° resolution) provided by Japan Meteorological Agency (JMA) and CPC Merged Analysis of Precipitation (CMAP, Xie and Arkin 1997, 2.5° resolution) were used to verify 1986-2003 in both AGCMs at all resolutions. Furthermore, we used Global Precipitation Climatology Project version 1.2 (GPCP, Huffmann et al. 2001, 1° resolution) in Section 4.2 to verify synoptic rainfall variability and Tropical Rainfall Measuring Mission product 3B43v7 (TRMM, Huffman et al. 2007, 0.25° resolution) in Section 4.1 to verify rainfall over orography. In these two observational datasets, due to data coverage, different periods (1997-2012 in GPCP, and 1998-2012 in TRMM) were analyzed. Except in Section 4.1, all datasets were re-gridded to N96 (approximately 200-km resolution).

2.3. Analysis methods

In Section 3, we used Taylor's skill scores to evaluate the model performance. Using pattern correlation (R) and standard deviation ratio (SDR; GCM's value normalized by observed value), Taylor (2001) proposed a skill score (S) to evaluate the

GCM reproducibility,

$$S = \frac{4(1+R)^4}{(SDR + 1/SDR)^2(1+R_0)^4}, R_0 \rightarrow 1 \ldots (1).$$

. Higher S means higher reproducibility and if a GCM's performance is perfect (SDR→1 and R→1), S = 1.

In Section 4.2, to investigate the resolution sensitivity of the intra-seasonal variability, we define the BSISO index (21-61 day rainfall variability over 12-22°N, 70-95°E) and calculate the lag covariance of intra-seasonal rainfall variability (21-61 day band-passed) onto the BSISO index (Ajayamohan et al. 2009) to assess the characteristics of northward propagation of BSISO during boreal summer (Figure 10).

3. Resolution sensitivity of the ASM seasonal mean

First, in the ASM seasonal mean, we compare the June-July-August (JJA) climatology of precipitation and 850 hPa circulation in MRI-AGCM and MetUM. TL95 MRI-AGCM and N96 MetUM (Figure 1a and 1c) shows similar clockwise ASM circulation at 850 hPa. However, their JJA precipitation pattern is quite different. In TL95 MRI-AGCM, the precipitation maximum is over the Indian subcontinent and South Asia, while in N96 MetUM, precipitation peaks in the equatorial Indian Ocean. The difference between the AGCM biases (defined as 'AGCM minus CMAP') in MRI-AGCM and MetUM is shown in Fig. 1b and 1d. Over the tropical Indian Ocean, dry (wet) bias exists near the equator while wet and cyclonic (dry and anticyclonic) bias appears over the northern hemisphere in MRI-AGCM (MetUM). Over the western

Pacific, cyclonic bias appears south of Japan in both MRI-AGCM and MetUM.

Next, we investigate the resolution sensitivity of precipitation over the south Asian monsoon domain. In MRI-AGCM, dry bias over the tropical Indian Ocean is improved (Fig. 2a-2c). For example, mean bias over the tropical Indian Ocean (20°S-20°N, 40-100°E) is 0.62 mm day^{-1} in TL95 and -0.19 mm day^{-1} in TL959 (Fig. 3a). On the other hand, the root mean square error (RMSE) (2.6 mm day^{-1} in TL95 and 3.1 mm day^{-1} in TL959) and the pattern correlation (0.80 in TL95 and TL959) are not improved (Fig. 3b and 3c). This is probably because some places show improvements, but others do not and may even degrade, so the scores do not change. In MetUM, the meridional dipole bias over the tropical Indian Ocean (wet bias on the equator and dry bias around 10-20°N) is improved (Fig. 2d-2f). However, on the basin-wide average (20°S-20°N, 40-100°E), mean bias (0.12 mm day^{-1} in N96 and 0.08 mm day^{-1} in N512), RMSE (3.9 mm day^{-1} in N96 and 3.6 mm day^{-1} in N512), and pattern correlation (0.60 in N96 and 0.62 in N512) are not substantially improved (Fig. 3a-3c). Taylor's skill scores also show that the scores are not improved in both MRI-AGCM and MetUM (Fig. 4a). Consistent with Johnson et al. (2016)'s results, the resolution sensitivity decreases as resolution increases, so the resolution sensitivity of precipitation and 850 hPa circulation is larger from TL95 to TL319 in MRI-AGCM (N96 to N216 in MetUM), than from TL319 to TL959 in MRI-AGCM (N216 to N512 in MetUM) (Fig. 2). Resolution sensitivity of precipitation is different between MRI-AGCM and MetUM, with a pattern correlation of 0.22 (0.21-0.24 in Jackknife method) over the Indian Ocean (20°S-20°N, 40-100°E). In MRI-AGCM, large off-equatorial precipitation increase appears both north and south of the equator. Particularly, a large precipitation increase can be seen over the west of the Western Ghats and a cyclonic anomaly appears over the Arabian Sea (Fig. 2a-2c). Precipitation also increases with resolution over the northern Indian subcontinent and southern Indian Ocean around 0-10°S. In MetUM, this off-equatorial precipitation increase with resolution is less significant and a precipitation decrease appears over the equator (Fig. 2d-2f).

MRI-AGCM and MetUM share a similar resolution sensitivity of precipitation over the western Pacific (Fig. 2c and 2f), with a pattern correlation of 0.48 (0.41-0.53 in Jackknife method) over the western Pacific (0-40°N, 120-180°E). At higher resolution, precipitation decreases over the northwestern Pacific and northern MC, while it increases over East Asia (around 20-40°N) and the southern MC., An anticyclonic circulation change associated with the precipitation decrease also appears over the northwestern Pacific. Such anticyclonic circulation transports moisture from the tropics to the East Asia and reinforces the Baiu-Meiyu front, which is consistent with previous studies showing that high-resolution AGCMs can reproduce a more realistic Baiu-Meiyu rainband (Kitoh and Kusunoki 2008). Taylor's skill scores (Fig. 4c) quantitatively show that the scores over the Baiu-Meiyu front (20-40°N, 120-150°E) are improved in both MRI-AGCM (0.20 in TL95 and 0.50 in TL959) and MetUM (0.20 in N96 and 0.27 in N512).

In order to investigate the resolution sensitivity of precipitation, we analyze the moisture budget at different resolutions (Figures 5 through 7). Fig. 5a and 5e show JJA climatology of TL95 MRI-AGCM and N96 MetUM moisture transport and convergence. The clockwise moisture transport of ASM occurs in both models. On the other hand, moisture convergence maximum over the Indian subcontinent appears in MRI-AGCM, while convergence stays over the equatorial Indian Ocean in MetUM. Over the southern MC, MetUM shows a large increase in moisture convergence (Fig. 5h), which is less significant in MRI-AGCM (Fig. 5d). Moisture budget analysis also exhibits these features (Fig. 6d). Compared to the moisture convergence changes, surface evaporation increases only slightly with resolution over the MC in MRI-AGCM, while it does not change in MetUM (Fig. 6c). Over the northern Indian Ocean, similar to the pattern of precipitation change (Fig. 2), a large moisture convergence increase occurs over the west of the Western Ghats and Northern Indian Ocean in MRI-AGCM (Fig. 5d), while this is less significant in the MetUM where increased divergence appears over the equator (Fig. 5h). It should be noted that westward moisture flux anomaly appears over the South China Sea and Bay of Bengal in both models, which is probably related to the anticyclonic circulation anomaly seen in Fig. 2 and the decreased diabatic heating in the west Pacific.

Johnson et al. (2016) showed in the MetUM that decreasing precipitation over the northern Maritime Continent/west Pacific and increasing precipitation over the southern Maritime Continent were related to changes in moisture flux convergence. Following their study, we applied an area-integrated moisture budget analysis over their Maritime Continent regions and show the results in Figure 6b-6d. In MRI-AGCM, the precipitation decrease (and moisture convergence decrease) with resolution is consistent with MetUM over the northern box. In MRI-AGCM (MetUM), precipitation decreases from 9.67 mm day^{-1} in TL95 (7.73 mm day^{-1} in N96) to 8.73 mm day^{-1} in TL959 (6.22 mm day^{-1} in N512). Moisture convergence in MRI-AGCM (MetUM) also decreases with increasing resolution: 5.05 mm day^{-1} in TL95 (3.01 mm day^{-1} in N96) to 4.11 mm day^{-1} in TL959 (1.85 mm day^{-1} in N512). In contrast, precipitation and moisture convergence tendencies in southern box are different between these AGCMs. In MetUM, the precipitation increase from 5.5 mm day^{-1} in N96 to 6.5 mm day^{-1} in N512 is mainly due to an increase in moisture convergence (0.5 mm day^{-1} in N96 and 1.5 mm day^{-1} in N512). On the other hand, precipitation (5.2 mm day^{-1} in TL95 and 5.3 mm day^{-1} in TL959) and moisture convergence (0.3 mm day^{-1} in TL95 and TL959) are not sensitive to resolution in MRI-AGCM.

To examine the difference in the resolution sensitivity of precipitation in the Indian Ocean, we also perform a moisture budget analysis for the regions outlined in Fig. 6a. Over the southern Indian Ocean (around 60-90°E, 0-10°S), the precipitation increase is more significant in MRI-AGCM than in MetUM. Over the Northern Indian Ocean (Fig. 6e-6g), increasing precipitation (and increasing moisture convergence) is clear in MRI-AGCM. High-resolution MetUM also shows a slight precipitation and moisture convergence increase in the northern box. However, there are large inter-model differences in the low-resolution climatology in these two models. Moisture converges (diverges) over the northern (southern) region in MRI-AGCM while the opposite occurs in MetUM (Fig. 6e-6g).

To investigate the origin of the different behavior of moisture budget over the southern MC, Figure 7 shows averaged moisture flux into and out of the southern/northern MC and equatorial IO boxes (Fig. 7a). In MetUM, the increase of moisture in finer-resolution over the southern MC is mainly caused by the decrease of cross equatorial moisture flux (Fig. 7e-7g). On the other hand, in MRI-AGCM, change of cross equatorial moisture flux is smaller than in MetUM (Fig. 7b-7d). Furthermore, difference in the moisture supply across 160°E and moisture loss across 90°E seems important. Across 160°E, moisture supply decreases (increases) in MRI-AGCM (MetUM) with higher resolution, which partly contributes to the different resolution sensitivity of moisture convergence between two AGCMs over the southern MC box.

This difference over the southern MC may be related to differences in the southern IO. In MRI-AGCM, budget of southern equatorial IO box shows distinct decrease of cross equatorial moisture flux, which causes increase of moisture particularly from TL95 to TL319 (Fig. 7c). Moisture flux across 90°E increases (decreases) moisture over the southern equatorial IO (southern MC).

4. What contributes to the resolution sensitivity of the ASM seasonal mean?

The previous section motivates a question: why is the resolution sensitivity of precipitation similar over the MC and west Pacific, but different over the Indian Ocean and India in the two models? To answer this, we examine possible mechanisms driving the resolution sensitivity, including better resolution of orography, better resolution of intraseasonal/synoptic variability and the resolution sensitivity of the meridional temperature gradient that drives the monsoon.

4.1. Orography

High-resolution AGCMs are able to represent steep topography over south Asia (Figure 8) and MC (Figure 9), which may affect the simulation of precipitation and circulation. In both MRI-AGCM and MetUM, sharper rainfall peaks appear on the western side of mountains at higher resolutions (Fig. 8b and 8d). The monsoon westerly wind intersects the Western Ghats (75°E), Arakan Yoma (90-95°E), Bilauktang (100°E), Annam Cordillera (110°E), and Cordillera Central (120°E). Precipitation is clearly intensified around these mountains in TL959 and TL319 in MRI-AGCM (N512 and N216 in MetUM), while TL95 MRI-AGCM and N96 MetUM cannot represent such steep orography and the precipitation is smoothed (Fig. 8). Orography-induced precipitation can be also seen in the MC. Fig. 9 shows that rainfall increases over the mountains of New Guinea in the high-resolution AGCMs (around 5°S, Fig. 9b and 9d). Although there is observation uncertainty, AGCMs are too wet over the land because of the orography (Fig. 9b and 9d). The spatial distribution of precipitation over this area is probably better at high resolution, but precipitation is more intense because of the steepness of the mountains, causing a larger drag. High-resolution observation (TRMM) also shows orography-induced rainfall, which can not be reproduced in coarse-resolution AGCM (Fig. 8 and 9).

As mentioned in Section 3, in both models, rainfall decreases north of the Maritime Continent. Johnson et al. (2016) hypothesized that increased resolution of the orography of the Maritime Continent and Indochina created this precipitation decrease through increasing moisture convergence over the orography, which reduces the westerly and southerly moisture transport into the west Pacific. As mentioned in Section 3, the resolution sensitivity of westerly moisture flux into the northern Maritime Continent is larger in the MRI-AGCM than the resolution sensitivity of southerly moisture flux. In the MRI-AGCM, the change in westerly moisture flux could be related to the increased rainfall in the Indian Ocean basin. The lack of a precipitation increase over the southern Maritime Continent in MRI-AGCM is likely due to the increase in moisture convergence over the southern Indian Ocean, which is not present in MetUM. It is not clear whether the same mechanisms are leading to the decrease in precipitation in the west Pacific in both GCMs, and this would be an interesting subject for future sensitivity experiments.

4.2. Synoptic and Intra-seasonal variations over India

Intra-seasonal variability can be decomposed into three modes: BSISO (21-61 day; Yasunari 1980, Jiang et al. 2004, Ajayamohan et al. 2009), biweekly-mode (9-21 day; Murakami 1976, Krishnamurti and Ardanuy 1980, Annamalai and Slingo 2001), and LPS (3-9 day; Mak 1987, Goswami et al. 2003). The lead-lag covariance of precipitation over 70-95°E onto the BSISO index exhibits the characteristics of northward propagation of BSISO during boreal summer (Figure 10). The northward propagation with about 50-day period is clear in both MRI-AGCM and MetUM (Fig. 10a-10d), consistent with previous studies (Ajayamohan et al. 2009). In MetUM, there is little difference in the BSISO propagation between N96 (Fig. 10c) and N512 (Fig. 10d). In MRI-AGCM, BSISO rainfall in TL959 (Fig. 10b) shifts slightly northward (around 20°N) compared to TL95 (Fig. 10a), but there is little change in amplitude. Therefore, the BSISO activity has very little resolution sensitivity in either GCM.

Another possible driver of the resolution sensitivity of rainfall and circulation is synoptic variability. For example, high-resolution AGCMs often improve the representation of LPS over the northern Indian Ocean (Stowasser et al. 2009, Sabin et al. 2013, Johnson et al. 2016). Figure 11 shows the standard deviation of synoptic-timescale (3-9 day band-passed) rainfall variability. The intra-seasonal variability over central India increases substantially in the high-resolution (TL959) MRI-AGCM (Fig. 11c). In N512 MetUM, synoptic timescale variability increases (decreases) slightly over Bangladesh (ocean, e.g. Bay of Bengal), which is consistent with the shift of the synoptic systems (Fig. 11f), shown using LPS tracking in Johnson et al. (2016). The larger increase synoptic variability in MRI-AGCM than in MetUM partly explains why the resolution sensitivity of precipitation is different in the two GCMs over India and the Indian Ocean. An increase in LPS increases condensation heating over India and the atmospheric response to this heating can increase the moisture transport to the continent. These processes may act as a positive feedback to enhance the precipitation. Observed daily precipitation (GPCP, 1997-2012) in Figure 12 shows that too much (little) synoptic rainfall variability appears over the southern (northern) subcontinent in TL95 MRI-AGCM (Fig. 12b) while synoptic rainfall variability is generally too small over India in N96 MetUM (Fig. 12c). The resolution sensitivity of LPS (Fig. 11), has the opposite sign of the bias, particularly in the MRI-AGCM, and consequently improves the bias of synoptic rainfall variability over

India.

4.3. Upper tropospheric warming

Meridional thermal gradient (MTG) in the upper troposphere is a major driver of the south Asian monsoon (e.g. Li and Yanai 1996, Xavier et al. 2007). In boreal summer, warming over the south Asian continent causes reversal of the MTG and can be used to define a south Asian monsoon (SAM) onset date. To investigate the resolution sensitivity of the upper tropospheric warming, the resolution sensitivity of the 200-600 hPa tropospheric thickness is shown in Figure 13. As resolution increases, tropospheric cooling appears over the tropics (from 30°S to 30°N) in MRI-AGCM and over the Indo-Pacific in MetUM. Over the northwestern Pacific (NWP) and South China Sea (SCS) region (0-20°N, 105-180°E), 200-600 hPa thickness change is larger in MRI-AGCM (-23.08 m in MRI-AGCM, while -5.02 m in MetUM, equal to 21.8% of MRI-AGCM). Such cooling seems to originate from the NWP, consistent with rainfall decrease and anti-cyclonic anomaly. Tropospheric cooling spreads into the entire tropics zonally, and this enhances land-sea thermal contrast over the South Asian continent. Such thermal contrast change is larger in MRI-AGCM (Fig. 13a-c) than in MetUM (Fig. 13d-f).

To diagnose whether the resolution sensitivity of heating over the NWP is important for this tropospheric cooling response, we investigate the Matsuno-Gill like response (Matsuno 1966, Gill 1980) to regional heating using a linear baroclinic model (LBM), similar to Ogata (2013). LBMs are derived from the linearized atmospheric primitive equation using a sigma coordinate system. The LBM used here has a rest background state (i.e. zero background velocity), a zonally averaged equatorial thermal structure (i.e. uniform stratification) derived from JRA-55, and a resolution of 2.5° horizontally with 14 vertical levels. Heating was estimated for each model individually from the precipitation pattern seen in Fig. 2c and 2f, and is shown in Figure 14 a and c. To define the vertical profile, a heating maximum of 0.47 K day^{-1} per 1 mm day^{-1} is assumed at 600 hPa and the heating reachs zero at 200 and 1000 hPa. Figure 14 shows the response to the change in heating when resolution is increased in the MRI-AGCM and MetUM. In MRI-AGCM and the MetUM, response to western Pacific forcing (30°S-30°N, 120-180°E in Fig. 14a, c) contributes to tropospheric cooling on 200-600 hPa due to the rainfall decrease (Fig. 14b, d), but in the MetUM the response is much weaker. It should be noted that key features of tropospheric cooling in Fig. 13 (e.g. larger tropospheric cooling in MRI-AGCM) cannot be reproduced in this linear model by the Indian Ocean forcing (not shown). Particularly the effect of warming by the Indian Ocean forcing may be overestimated.

Figure 15 shows the seasonal evolution of MTG, as defined by Xavier et al. (2007): the difference between the 200-600 hPa upper tropospheric thickness (units: m) averaged over south Asia (5-35°N, 40-100°E) and the equatorial Indian ocean (15°S-5°N, 40-100°E). In both MRI-AGCM and MetUM, the MTG changes sign from negative to positive between May and June. During May-June, the MTG is stronger in TL959 MRI-AGCM than in TL95 MRI-AGCM, and similarly MTG in N512 MetUM is stronger than in N96 MetUM. Interestingly, resolution sensitivity is comparable in magnitude to the inter-model difference (Fig. 15). During August-September, in contrast, there is little resolution sensitivity and the inter-model difference is larger. In reanalysis (JRA-55), sign reversal of MTG starts earlier and the MTG is larger throughout the season. This means the higher-resolution GCMs are more accurate (Fig. 15) than the low-resolution. The stronger MTG in the high-resolution MRI-AGCM is likely related to the increasing SAM precipitation. MTG is also linked to the easterly vertical wind shear between U850 and U200, which contributes to synoptic variability through an internal instability condition (Charney and Stern 1962, Shukla 1978). The larger MTG in the high-resolution MRI-AGCM may consequently be related to the increase in synoptic variability seen in Fig. 11 and the associated with increased precipitation from monsoon LPS.

5. Summary and discussion

In this study, the resolution sensitivity of the ASM in two AGCMs, MRI-AGCM and MetUM, is investigated and compared. We compare the MetUM series at N96 (200-km mesh on the equator), N216 (90-km mesh) and N512 (40-km mesh), with the MRI-AGCM series at TL95 (180-km mesh on the equator), TL319 (60-km mesh) and TL959 (20-km mesh).

Both MRI-AGCM and MetUM share a similar precipitation decrease over the western Pacific with increasing resolution. Associated with the precipitation decrease, low-level anti-cyclonic circulation change appears over the northwestern Pacific. On the other hand, over the Indian Ocean, the resolution sensitivity of precipitation is quite different between the two AGCMs. In MRI-AGCM, a large precipitation increase appears off the equator, while such off-equatorial precipitation increase is less significant and precipitation decreases over the equator in MetUM. The resolution sensitivity is not a clear improvement on the mean state in either GCM, and the resolution sensitivity is not proportional to the GCM bias. To examine the difference in the resolution sensitivity of precipitation, we also performed a moisture budget analysis. Over the Indian Ocean, there are large inter-model differences in the low-resolution climatology in these two models. Moisture converges (diverges) over the northern (southern) region in MRI-AGCM while the opposite occurs in MetUM. Over the Maritime Continent, decrease of cross equatorial moisture flux which is important for precipitation in MetUM (Johnson et al. 2016) is small in MRI-AGCM.

As possible causes of the resolution sensitivity of the ASM, orographic effect, intra-seasonal variability, and changes to the meridional temperature gradient have been considered. Both high-resolution AGCMs (TL959 and N512) can represent steep topography, which anchors rainfall pattern over south Asia and the Maritime Continent. Furthermore, increase of synoptic rainfall variability by low pressure systems at TL959 and N512 seems to contribute to the rainfall increase over the land, but is much more significant in the MRI-AGCM. Additionally, an upper-tropospheric cooling over the tropics, linked to rainfall and diabatic heating changes over the west Pacific (Section 4.3), causes a stronger meridional thermal gradient at high resolution, particularly in MRI-AGCM, and improves the seasonal evolution of the MTG. The larger resolution sensitivity of LPS and the MTG in the MRI-AGCM than the MetUM may be related, and likely contribute to the larger resolution sensitivity of Indian precipitation in the MRI-AGCM.

There are, however, large differences in circulation and precipitation over the Indian Ocean between MRI-AGCM and MetUM. On the equatorial Indian Ocean, there is a negative rainfall anomaly in MRI-AGCM. In contrast, a positive rainfall anomaly appears around 10-20°N (Figure 16). These results suggest that the anti-symmetric meridional dipole anomaly over the Indian Ocean generates a clockwise circulation and, in presence of a positive feedback, the westerly response to the diabatic heating around 10-20°N further generates a condensation heating through moisture supply over south Asia. Such mean state difference in the Indian monsoon between MRI-AGCM and MetUM may cause the different resolution sensitivity through the interaction with topography (e.g. larger rainfall increase in MRI-AGCM than in MetUM on the western side of the mountains; Fig. 2 and 8), and synoptic intra-seasonal variability by moist instability (e.g. different patterns in synoptic rainfall variability between MRI-AGCM and MetUM; Fig. 11). It should be noted that the inter-model difference becomes smaller at high resolution over the equatorial Indian Ocean (Fig. 16b and 16c).

In Section 4.1 and 4.2, we discussed orographic and non-orographic effects on resolution sensitivity. However, quantitative evaluation of their effect is still unclear. Sensitivity experiments would help quantify the relative importance of orographic and non-orographic effects. In MetUM, for example, previous study has reported that annual mean precipitation over the MC is sensitive to the representation of coastal lines through mean circulation change (Schiemann et al. 2014).

Our findings have highlighted some common features in the resolution sensitivity of the ASM simulation between the MetUM and the MRI-AGCM. However, we have also highlighted some major differences, which are likely due to the differences in the model physics schemes, which also cause different model mean biases. These results highlight the necessity of multi-model assessments regarding the role of resolution in climate simulations, such as the upcoming EU Horizon 2020 PRIMAVERA (PRocess-based climate sIMulation: AdVances in high-resolution modelling and European climate Risk Assessment) project.

Acknowledgements

SJJ and RS were supported by the Joint Weather and Climate Research Programme (JWCRP), a partnership between the Natural Environment Research Council (NERC) and the UK Met Office, under University of Reading Contract R8/H9/37. RS and MED were supported by the National Centre for Atmospheric Science Climate directorate (NCAS-Climate), a collaborative centre of NERC. MED acknowledges NCAS Climate contract R8/H12/83/001 for the High Resolution Climate Modelling programme. The MetUM simulations analysed here were produced as part of the UPSCALE project (information about data access is available from the project website: http://proj.badc.rl.ac.uk/upscale). We thank the UPSCALE team (P.L. Vidale [PI], M. J. Roberts, M. S. Mizielinski, J. Strachan, RS, MED), the large team of model developers, infrastructure experts and all the other essential components required to conduct the UPSCALE campaign, in particular the PRACE infrastructure and the Stuttgart HLRS supercomputing centre, as well as the STFC CEDA service for data storage and analysis using the JASMIN platform. We also acknowledge use of the MONSooN system, a collaborative facility supplied under JWCRP, and HECToR, the UK national supercomputer. Numerical experiments of MRI-AGCM were executed on the Earth Simulator of the Japan Agency for Marine-Earth Science and Technology (JAMSTEC). This work was conducted under the SOUSEI Program of the Ministry of Education, Culture, Sports, Science, and Technology (MEXT) of Japan.

Reference

Ajayamohan RS, Rao SA, Luo J-J, Yamagata T (2009) Influence of Indian Ocean Dipole on boreal summer intraseasonal oscillations in a coupled general circulation model. J Geophys Res 114: D06119. doi:10.1029/2008JD011096

Annamalai H, Slingo JM (2001) Active/break cycles: Diagnosis of the intraseasonal variability of the Asian summer monsoon. Clim Dyn 18: 85–102

Chang CP, Zhang YS, Li T (2000) Interannual and interdecadal variations of the East Asian summer monsoon and tropical Pacific SSTs. Part I: Roles of the subtropical ridge. J. Clim 13: 4310–4325

Charney JG, Stern ME (1962) On the stability of internal baroclinic jets in a rotating atmosphere. J Atmos Sci 19(2): 159-172

Cho C, Li R, Wang SY, Yoon JH, Gillies RR (2015) Anthropogenic footprint of climate change in the June 2013 northern India flood. Clim Dyn 46: 1-9

Demory ME, Vidale PL, Roberts MJ, Berrisford P, Strachan J, Schiemann R, Mizielinski MS (2014) The role of horizontal resolution in simulating drivers of the global hydrological cycle. Clim Dyn 42(7-8): 2201-2225

Donlon CJ, Martin M, Stark J, Roberts-Jones J, Fiedler E, Wimmer W (2012) The operational sea surface temperature and sea ice analysis (OSTIA) system. Remote Sens Environ 116: 140-158

Endo H, Kitoh A, Ose T, Mizuta R, Kusunoki S (2012) Future changes and uncertainties in Asian precipitation simulated by multiphysics and multi-sea surface temperature ensemble experiments with high-resolution Meteorological Research Institute atmospheric general circulation models (MRI-AGCMs). J Geophys Res 117: D16118. doi:10.1029/2012JD017874

Gill A (1980) Some simple solutions for heat-induced tropical circulation. Quart J Roy Meteor Soc 106(449): 447-462

Goswami BN, Ajayamohan RS, Xavier PK, Sengupta D (2003) Clustering of synoptic activity by Indian summer monsoon intraseasonal oscillations. Geophys Res Lett 30(8). doi: 10.1029/2002GL016734

Huffman GJ et al (2001) Global precipitation at one-degree daily resolution from multisatellite observations. J Hydrometeor 2(1): 36-50

Huffman GJ et al (2007) The TRMM multisatellite precipitation analysis (TMPA): Quasi-global, multiyear, combined-sensor precipitation estimates at fine scales. J Hydrometeor 8(1): 38-55

He C, Zhou T (2015) Decadal change of the connection between summer western North

Pacific Subtropical High and tropical SST in the early 1990s. Atmos Sci Lett 16: 253–259. doi: 10.1002/asl2.550

Jha B, Krishnamurti TN, Christides Z (2000) A note on horizontal resolution dependence for monsoon rainfall simulations. Meteor Atmos Phys 74(1-4): 11-17

Jiang X, Li T, Wang B (2004) Structures and mechanisms of the northward propagating boreal summer intraseasonal oscillation. J Clim 17: 1022–1039

Johnson SJ et al (2016) The resolution sensitivity of the South Asian monsoon and Indo-Pacific in a global 0.35° AGCM. Clim Dyn 46(3): 807-831

Joseph S et al (2015) North Indian heavy rainfall event during June 2013: diagnostics and extended range prediction. Clim Dyn 44(7-8): 2049-2065

Kitoh A, Kusunoki S (2008) East Asian summer monsoon simulation by a 20-km mesh AGCM. Clim Dyn 31(4): 389-401

Kobayashi C, Sugi M (2004) Impact of horizontal resolution on the simulation of the Asian summer monsoon and tropical cyclones in the JMA global model. Clim Dyn 23(2): 165-176

Kobayashi S et al (2015) The JRA-55 reanalysis: general specifications and basic characteristics. J Met Soc Jpn 93(1): 5-48

Krishnamurti TN, Ardanuy P (1980) The 10 to 20-day westward propagating mode and “Breaks in the Monsoons”. Tellus 32(1): 15-26

Kusunoki S, Mizuta R (2013) Changes in precipitation intensity over East Asia during the 20th and 21st centuries simulated by a global atmospheric model with a 60 km grid size. J Geophys Res 118(19). doi:10.1002/jgrd.50877

Lau WK, Kim KM (2012) The 2010 Pakistan flood and Russian heat wave: Teleconnection of hydrometeorological extremes. J Hydromet 13(1): 392-403

Li C, Yanai M (1996) The onset and interannual variability of the Asian summer monsoon in relation to land-sea thermal contrast. J Clim 9(2): 358-375

Liu P et al (2009) Tropical Intraseasonal Variability in the MRI-20km60L AGCM. J Clim 22(8): 2006-2022

Mak M (1987) Synoptic-scale disturbances in the summer monsoon. In: Monsoon Meteorology. Edited by Chang CP, Krishnamurti TN. Oxford Univ Press, pp 435–460

Martin GM (1999) The simulation of the Asian summer monsoon, and its sensitivity to horizontal resolution, in the UK Meteorological Office Unified Model. Quart J Roy Meteor Soc 125(557): 1499-1525

Matsuno T (1966) Quasi-geostrophic motions in the equatorial area. J Met Soc Jpn 44(1): 25-43

Mizielinski MS et al (2014) High-resolution global climate modelling: the UPSCALE project, a large-simulation campaign. Geosci Model Dev 7(4): 1629-1640

Mizuta R et al (2006) 20-km-mesh global climate simulations using JMA-GSM model-Mean climate states. J Met Soc Jpn 84(1): 165-185

Mizuta R et al (2012) Climate simulations using MRI-AGCM3.2 with 20-km grid. J Met Soc Jpn 2 90(0): 233-258

Murakami M (1976) Analysis of Summer Monsoon Fluctuations over India. J Met Soc Jpn 54: 15-31

Murakami H, Sugi M (2010) Effect of model resolution on tropical cyclone climate projections. SOLA 6: 73-76

Murakami H et al (2012) Future changes in tropical cyclone activity projected by the new high-resolution MRI-AGCM. J Clim 25(9): 3237-3260

Ogata T (2013) The Effect of the Australian-Maritime Continents on the Indian Ocean Dipole Mode in an Idealized Coupled General Circulation Model. SOLA 9(0): 84-88

Ogata T et al (2014) Projected future changes in the Asian Monsoon: A comparison of CMIP3 and CMIP5 model results. J Met Soc Jpn 92(3): 207-225

Oouchi K et al (2006) Tropical cyclone climatology in a global-warming climate as simulated in a 20 km-mesh global atmospheric model: Frequency and wind intensity analyses. J Met Soc Jpn 84(2): 259-276

Rayner NA et al (2003) Global analyses of sea surface temperature, sea ice, and night marine air temperature since the late nineteenth century. J Geophys Res 108(D14). doi: 10.1029/2002JD002670

Roberts MJ et al (2015) Tropical Cyclones in the UPSCALE Ensemble of High-Resolution Global Climate Models. J Clim 28(2): 574-596

Sabeerali CT, Ramu Dandi A, Dhakate A, Salunke K, Mahapatra S, Rao SA (2013) Simulation of boreal summer intraseasonal oscillations in the latest CMIP5 coupled GCMs. J Geophys Res 118(10): 4401-4420

Sabin TP, Krishnan R, Ghattas J, Denvil S, Dufresne JL, Hourdin F, Pascal T (2013) High resolution simulation of the South Asian monsoon using a variable resolution global climate model. Clim Dyn 41(1): 173-194

Schiemann R, Demory ME, Mizielinski MS, Roberts MJ, Shaffrey LC, Strachan J, Vidale PL (2014) The sensitivity of the tropical circulation and Maritime Continent precipitation to climate model resolution. Clim Dyn 42(9-10): 2455-2468

Shukla J (1978) CISK-barotropic-baroclinic instability and the growth of monsoon depressions. J Atmos Sci 35(3): 495-508

Sperber KR, Hameed S, Potter GL, Boyle JS (1994) Simulation of the northern summer monsoon in the ECMWF model: sensitivity to horizontal resolution. Mon Weather Rev 122(11): 2461-2481

Sperber KR, Annamalai H, Kang IS, Kitoh A, Moise A, Turner A, Wang B, Zhou T (2013) The Asian summer monsoon: an intercomparison of CMIP5 vs. CMIP3 simulations of the late 20th century. Clim Dyn 41(9-10): 2711-2744

Stephenson DB, Chauvin F, Royer JF (1998) Simulation of the Asian summer monsoon and its dependence on model horizontal resolution. J Met Soc Jpn 76(2): 237-265

Stowasser M, Annamalai H, Hafner J (2009) Response of the South Asian Summer Monsoon to Global Warming: Mean and Synoptic Systems. J Clim 22(4): 1014-1036

Taylor KE (2001) Summarizing multiple aspects of model performance in a single diagram. J Geophys Res 106(D7): 7183-7192

Vellinga M, Roberts M, Vidale PL, Mizielinski MS, Demory ME, Schiemann R, Strachan J, Bain C (2016) Sahel decadal rainfall variability and the role of model horizontal resolution. Geophys Res Lett 43. doi:10.1002/2015GL066690

Walters DN et al (2011) The Met Office Unified Model global atmosphere 3.0/3.1 and JULES global land 3.0/3.1 configurations. Geosci Model Dev 4(4): 919-941

Xavier PK, Marzin C, Goswami BN (2007) An objective definition of the Indian summer monsoon season and a new perspective on the ENSO–monsoon relationship. Quart J Roy Meteor Soc 133(624): 749-764

Xie P, Arkin PA (1997) Global precipitation: A 17-year monthly analysis based on gauge observations, satellite estimates, and numerical model outputs. Bull Amer Meteor Soc 78(11): 2539-2558

Xie SP, Xu H, Saji NH, Wang Y, Liu WT (2006) Role of Narrow Mountains in Large-Scale Organization of Asian Monsoon Convection. J Clim 19(14): 3420-3429

Yasunari T (1980) A quasi-stationary appearance of 30- to 40-day period in the cloudiness fluctuations during the summer monsoon over India. J Met Soc Jpn 58: 225–229

Yoshimura H, Mizuta R, Murakami H (2015) A spectral cumulus parameterization scheme interpolating between two convective updrafts with semi-Lagrangian calculation of transport by compensatory subsidence. Mon Weather Rev 143(2): 597-621

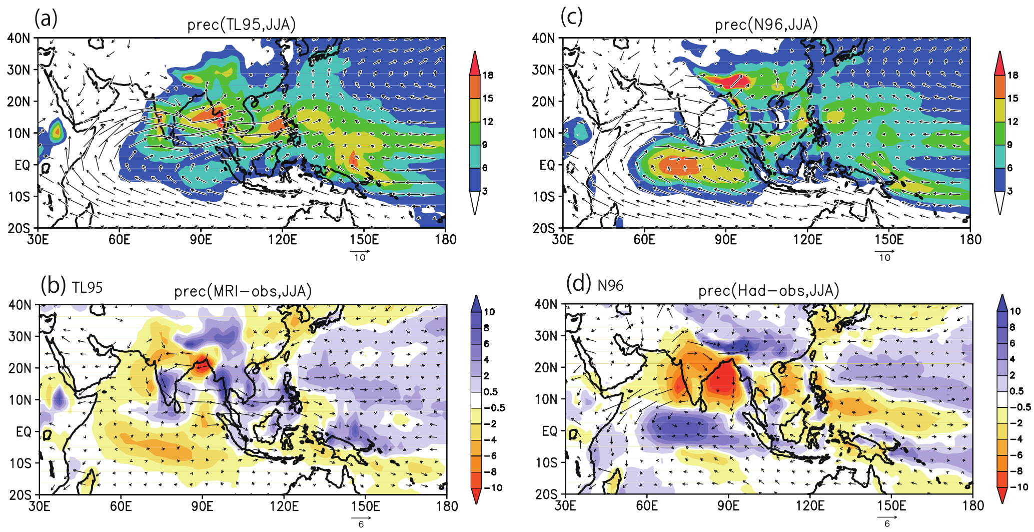

Figure 1: JJA precipitation (shaded, units: mm day^{-1}) and horizontal 850 hPa wind (vector, units: m s^{-1}) in (a) TL95 MRI-AGCM and (c) N96 MetUM. Difference between (b) TL95 MRI-AGCM, (d) N96 MetUM and CMAP observed precipitation / JRA-55 reanalysis wind.

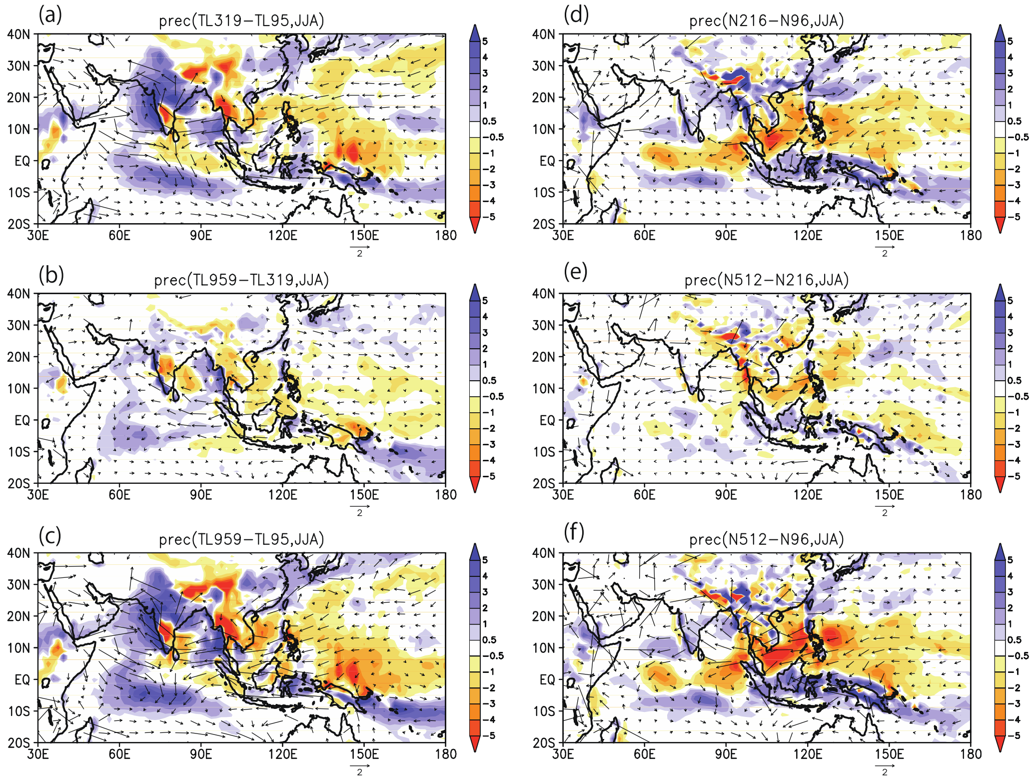

Figure 2: Resolution sensitivity of JJA precipitation (shaded, units: mm day^{-1}) and horizontal 850 hPa wind (vector, units: m s^{-1}) : (a) TL319-TL95, (b) TL959-TL319, and (d) TL959-TL95 MRI-AGCM. Right panels are same as (a)-(c) but for (d) N216-N96, (e) N512-N216, and (f) N512-N96 MetUM.

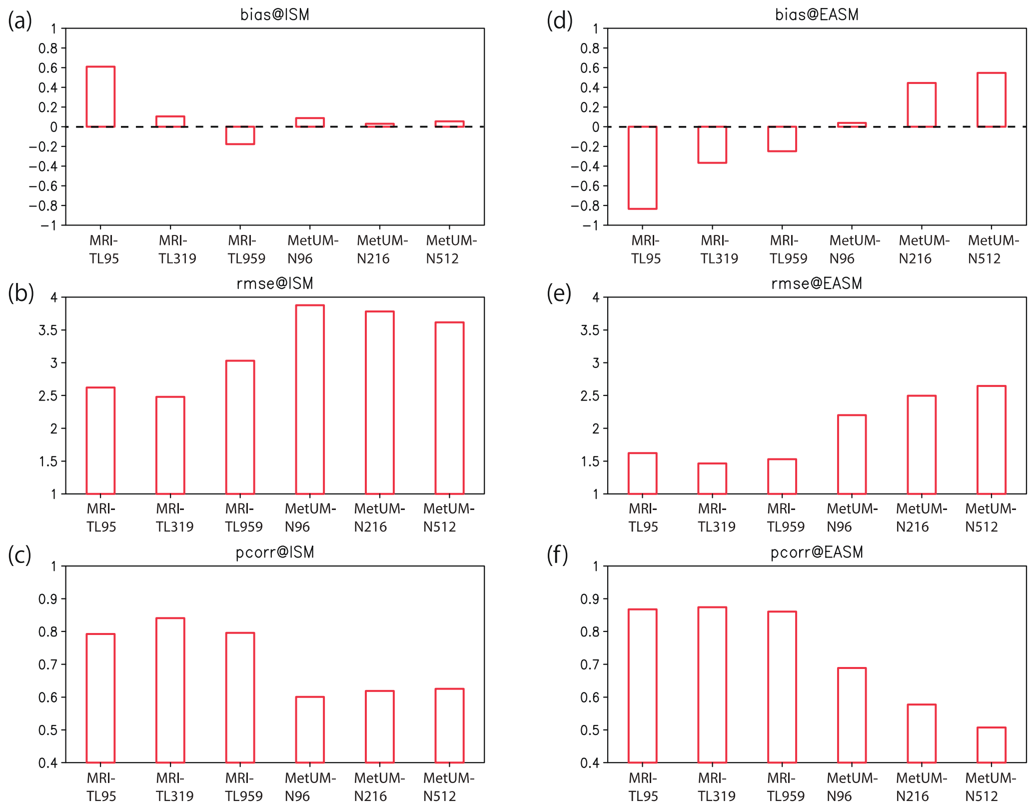

Figure 3: Area average over the tropical Indian Ocean (20°S-20°N, 40-100°E) of (a) mean JJA precipitation bias (units: mm day^{-1}), (b) RMSE, and (c) pattern correlation. (d)-(f) are same as (a)-(c) but for the western Pacific (0-40°N, 120-180°E). All datasets are re-gridded to CMAP resolution (2.5 degree). In (c) and (f), p-value at R=0.4 is $p < 0.00001$.

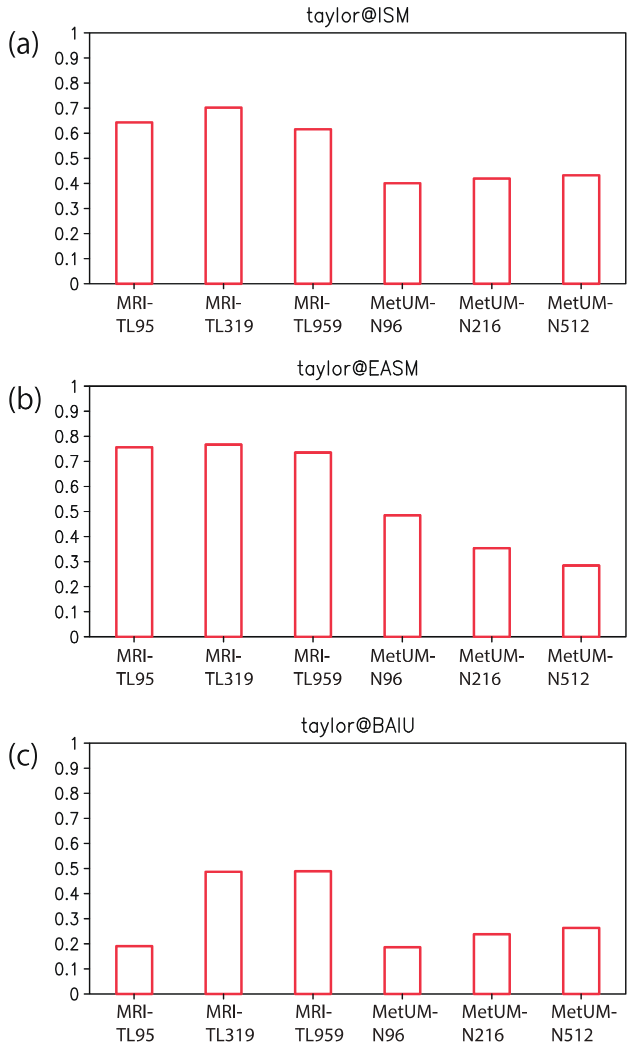

Figure 4: Taylor's skill scores (Taylor 2001) of JJA precipitation over (a) the tropical Indian Ocean (20°S-20°N, 40-100°E), and (b) the western Pacific (0-40°N, 120-180°E), and (c) Baiu-Meiyu front (20-40°N, 120-150°E). All datasets are re-gridded to CMAP resolution (2.5 degree).

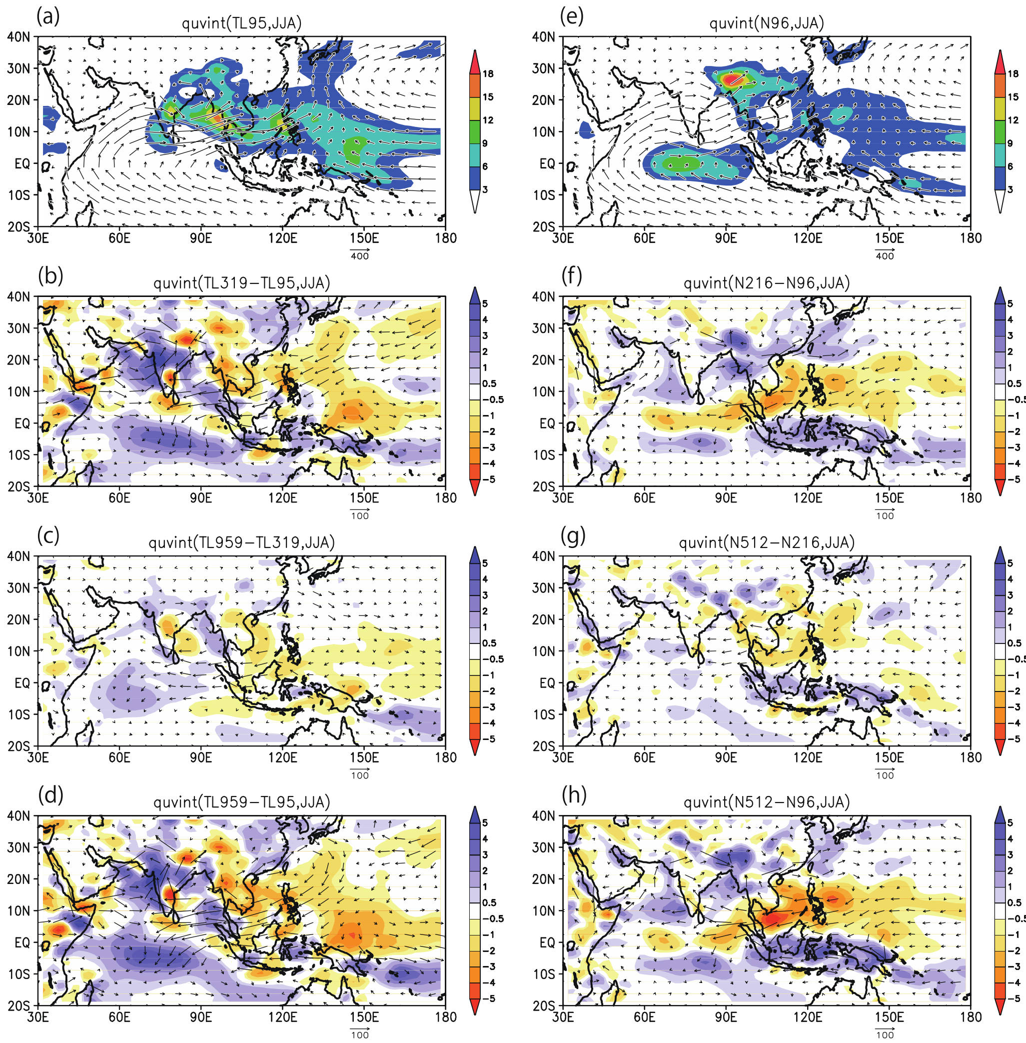

Figure 5: JJA vertical-integrated moisture flux (vector, units: kg $m^{-1}s^{-1}$) and its convergence (shaded, units: mm day^{-1}) in (a) TL95 MRI-AGCM, (b) TL319-TL95, (c) TL959-TL319, and (d) TL959-TL95. (e)-(h) are same as (a)-(d) but for (e) N96 MetUM, (f) N216-N96, (g) N512-N216, and (d) N512-N96.

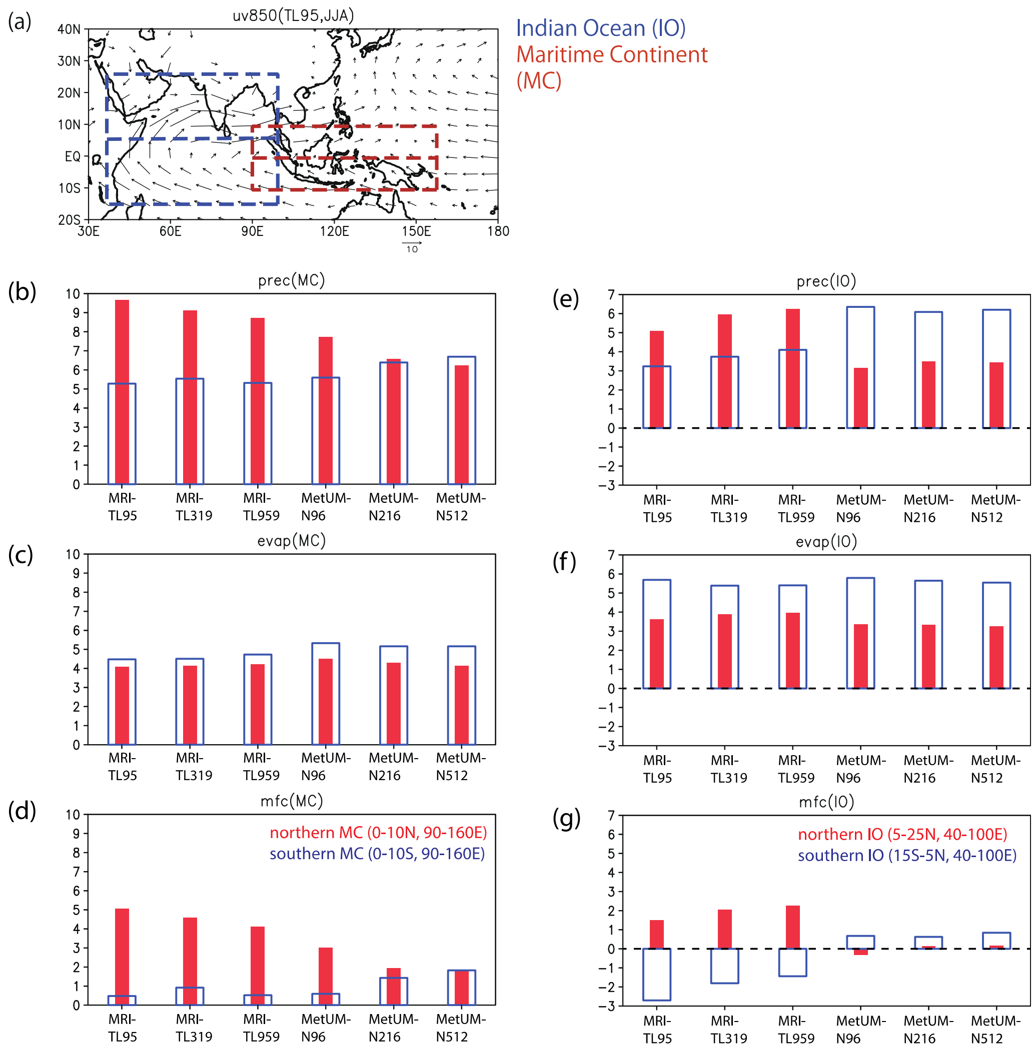

Figure 6: Resolution sensitivity of the JJA moisture budget over the regions outlined in (a) (units: mm day^{-1}): (b) precipitation, (c) surface evaporation, and (d) moisture flux convergence. Red and blue bars correspond to the northern (0-10°N, 90-160°E) and southern (0-10°S, 90-160°E) MC box regions, respectively. (e)-(g) are same as (b)-(d) for the Indian Ocean (IO) box region. Red and blue bars correspond to the northern (5-25°N, 40-100°E) and southern (15°S-5°N, 40-100°E) IO box regions, respectively.

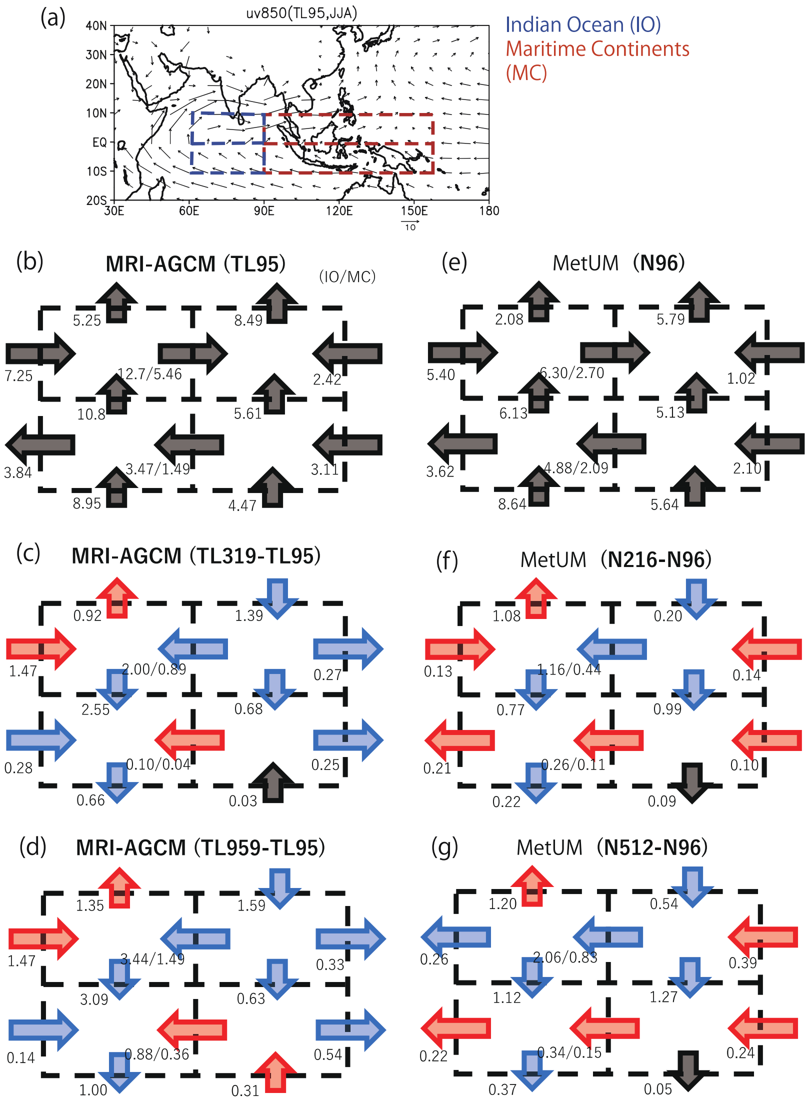

Figure 7: Resolution sensitivity of the JJA moisture flux across the borders shown in (a) (units: mm day^{-1}). Since this is an area average quantity there are two values at the borders between the Indian Ocean regions and Maritime Continent regions.: (b) TL95, (c) TL319-TL95, and (d) TL959-TL95 MRI-AGCM. (e) N96, (f) N216-N96, and (g) N512-N96 MetUM. Red (blue) arrows shows increase (decrease) of moisture flux.

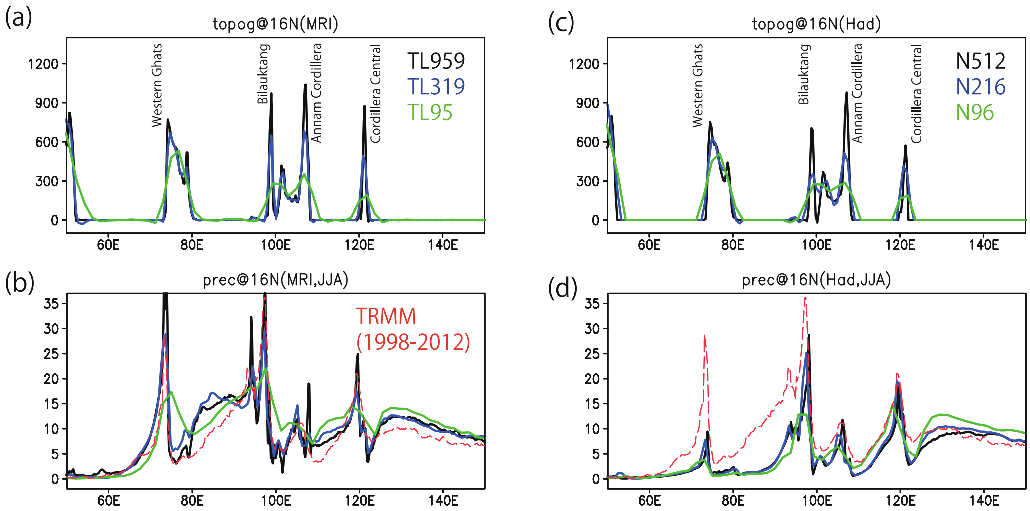

Figure 8: Zonal section at 16°N showing the resolution sensitivity of topography (units: m) in MRI-AGCM (a) and MetUM (c), and JJA precipitation (units: mm day^{-1}) in MRI-AGCM (b) and MetUM (d).

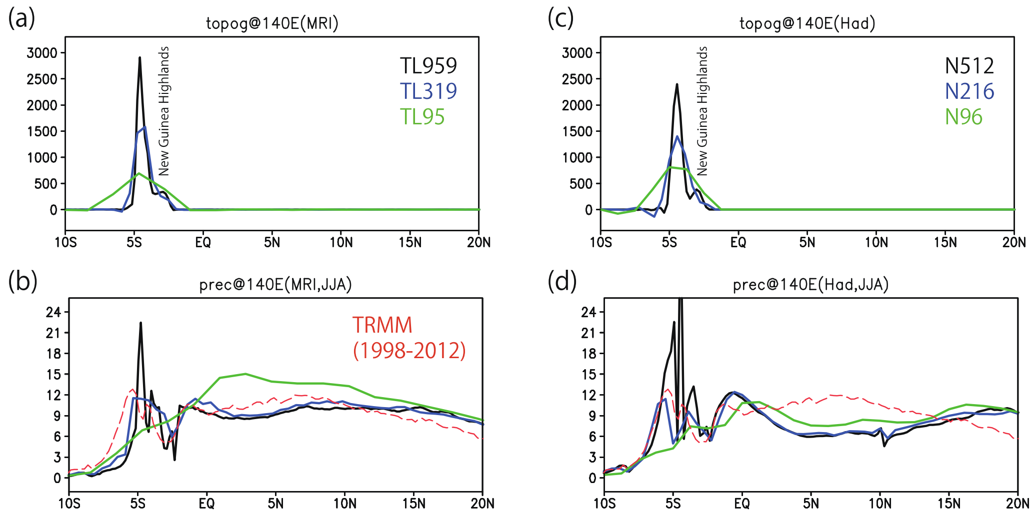

Figure 9: Same as Fig. 8, for a meridional section at 140°E.

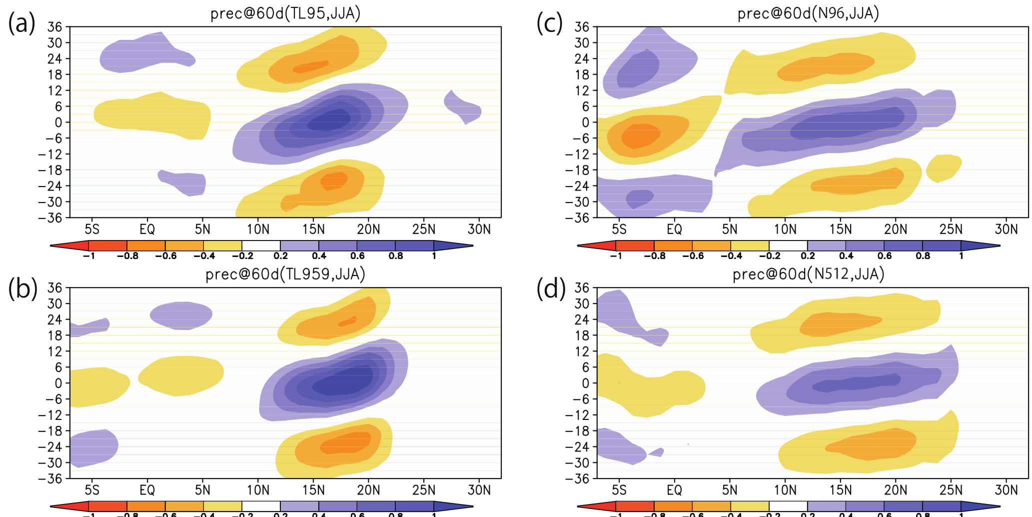

Figure 10: Latitude-time sections of lag covariance of intra-seasonal rainfall variability onto BSISO index (21-61 day rainfall variability over 12-22°N, 70-95°E during June-August) in (a) TL95 MRI-AGCM3, (b) TL959 MRI-AGCM3, (c) N96 MetUM, and (d) N512 MetUM. Units are mm day^{-1}. The covariance fields were normalized by the standard deviation of BSISO index.

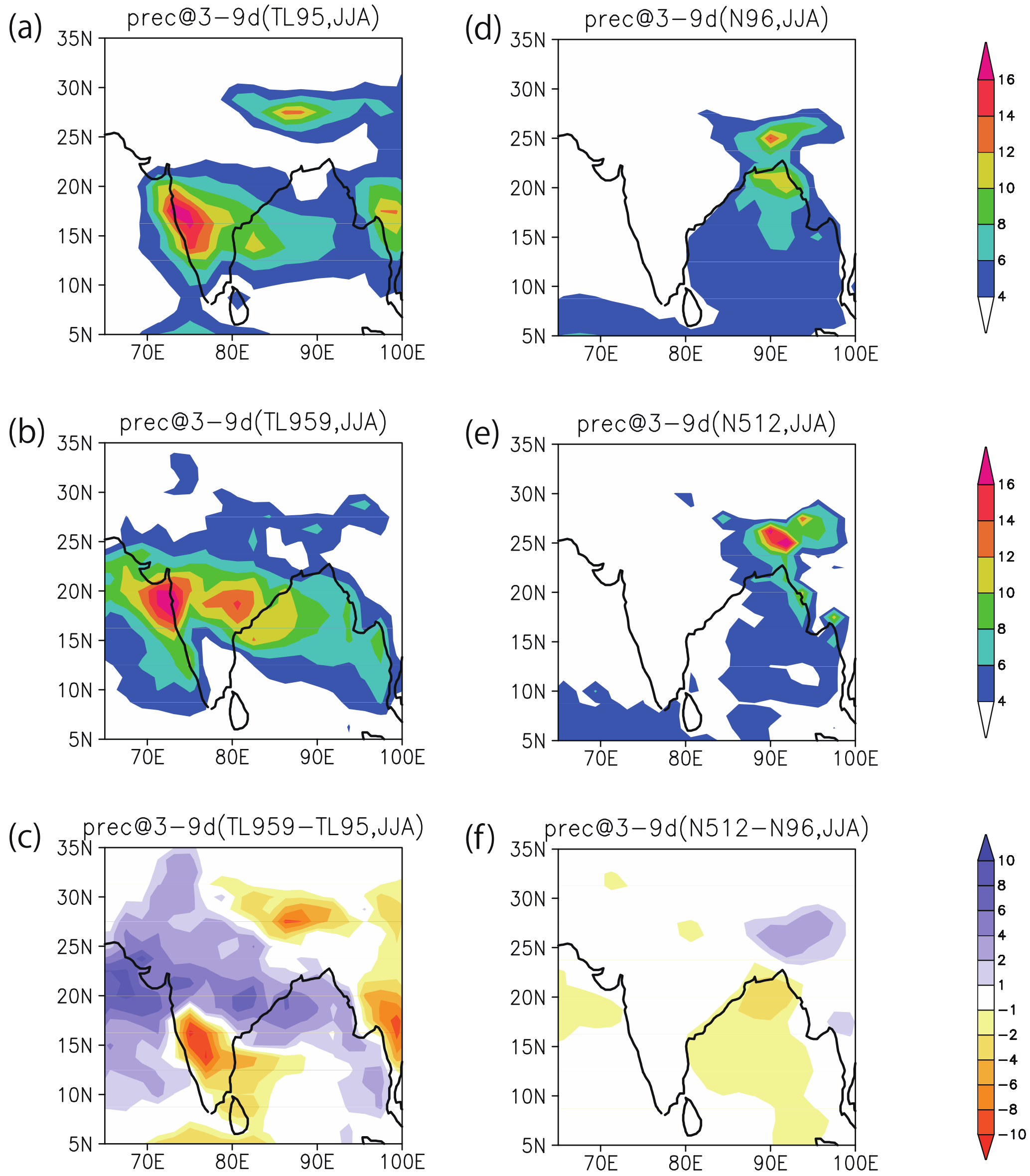

Figure 11: (a) Standard deviation of synoptic-scale (3-9 day band-passed) rainfall variability during JJA (shaded, units: mm day^{-1}) in (a) TL95, (b) TL959, and (c) its difference (TL959-TL95). (d)-(f) is same as (a)-(c) but for MetUM: (d) N96, (e) N512, and (f) its difference (N512-N96).

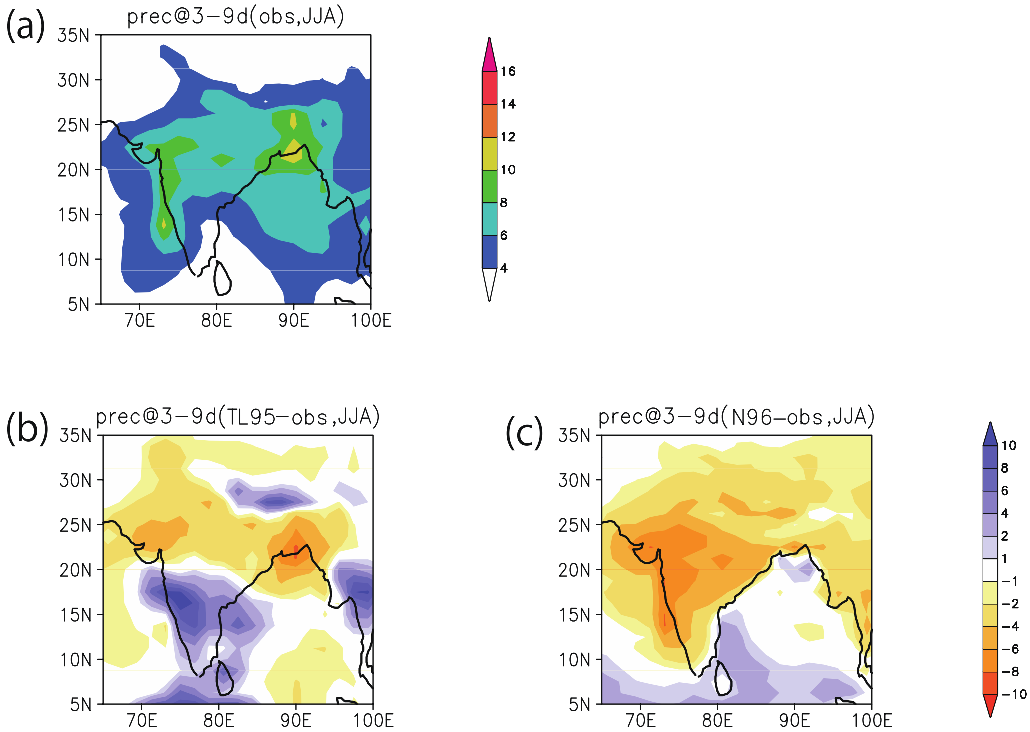

Figure 12: Same as Fig. 11 but for (a) GPCP daily observation (1997-2012), (b) TL95 MRI-AGCM minus GPCP, and (c) N96 MetUM minus GPCP.

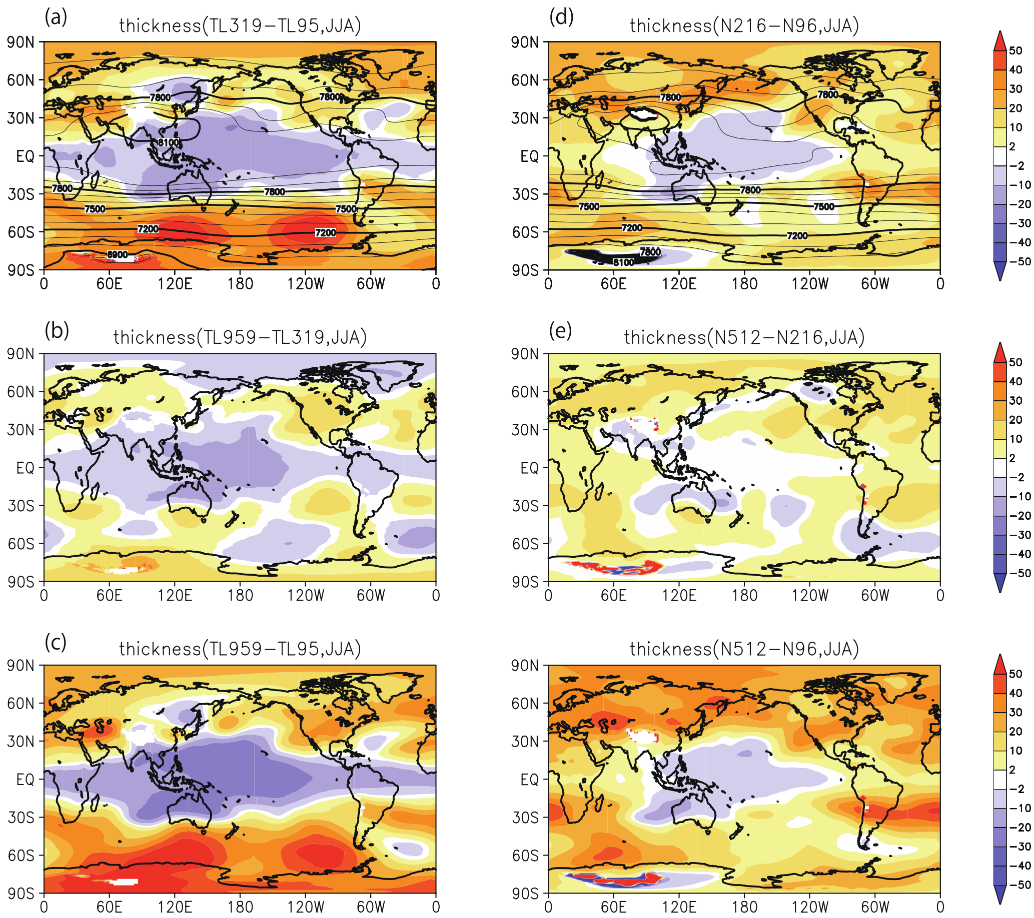

Figure 13: Differences in JJA 200-600 hPa upper tropospheric thickness (shaded, units: m): (a) TL319-TL95, (b) TL959-TL319, and (c) TL959-TL95 in MRI-AGCM. (d)-(f) are same as (a)-(c) but for (d) N216-N96, (e) N512-N216, and (f) N512-N96 in MetUM. Contours in (a) show upper tropospheric thickness in TL95 MRI-AGCM (units: m), and contours in (d) are for N96 MetUM.

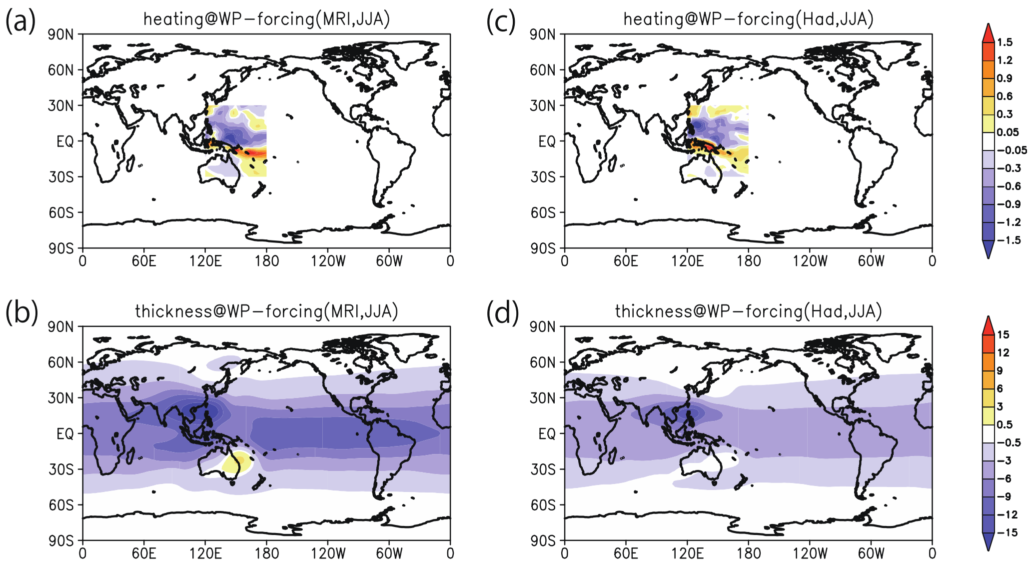

Figure 14: Responses (200-600 hPa thickness) to individual heating in MRI-AGCM and MetUM in a linear model. (a) Heating distribution (100-1000 hPa averaged, units: K day^{-1}) of western Pacific forcing (30°S-30°N, 120-180°E) and (b) response to the forcing (units: m) in MRI-AGCM. (c)-(d) are same as (a)-(b) but for MetUM.

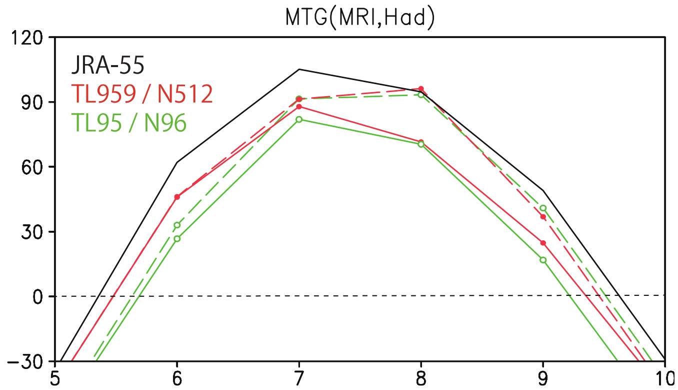

Figure 15: Seasonal evolution of monsoon temperature gradient (MTG, units: m) in Reanalysis (JRA-55, black solid line), MRI-AGCM (solid coloured lines) and MetUM (dash coloured lines). Higher resolution models are shown in red and lower resolution GCMs are shown in green.

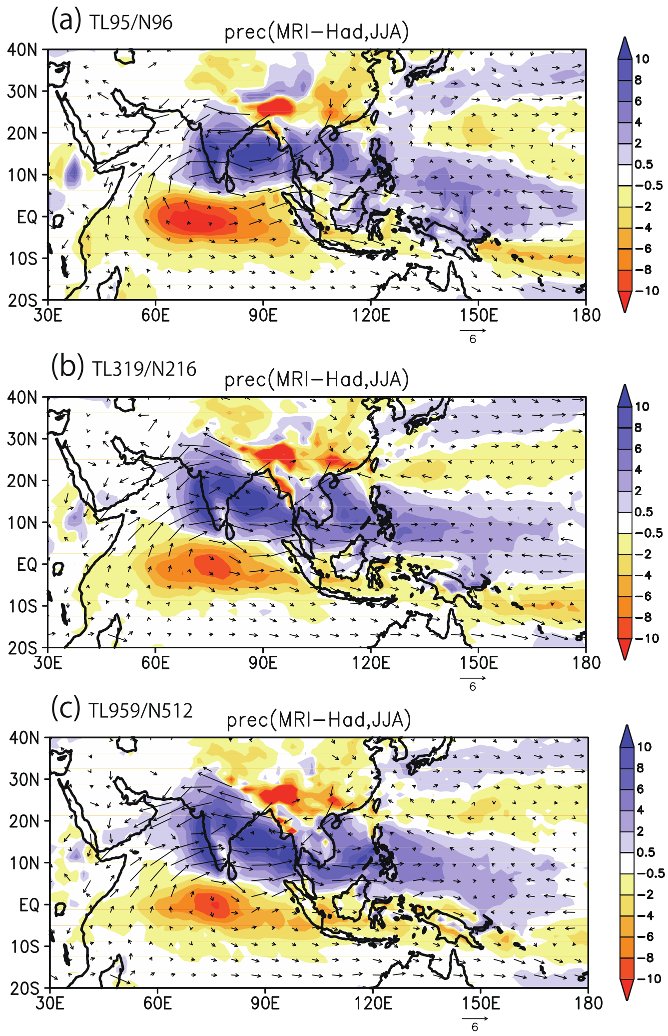

Figure 16: Difference in JJA precipitation (shaded, units: mm day^{-1}) and horizontal 850 hPa wind (vector, units: m s^{-1}) between the two GCMs compared in this study: (a)TL95 MRI-AGCM minus N96 MetUM, (b) TL319 MRI-AGCM minus N216 MetUM, and (c) TL959 MRI-AGCM minus N512 MetUM.